

See discussions, stats, and author profiles for this publication at: <https://www.researchgate.net/publication/280926651>

# Multisurface Interface Model for Analysis of Masonry Structures

Article in *Journal of Engineering Mechanics* · July 1997

DOI: 10.1061/(ASCE)0733-9399(1997)123:7(660)

---

CITATIONS

386

---

READS

230

2 authors, including:



Paulo B. Lourenco

University of Minho

776 PUBLICATIONS 7,860 CITATIONS

SEE PROFILE

Some of the authors of this publication are also working on these related projects:



Sustainable strengthening of masonry structures with textile reinforced mortars [View project](#)



Assessment of the influence of environmental conditions and structural damage in the dynamic behavior of historical adobe buildings through long-term monitoring [View project](#)

# MULTISURFACE INTERFACE MODEL FOR ANALYSIS OF MASONRY STRUCTURES

By Paulo B. Lourenço<sup>1</sup> and Jan G. Rots<sup>2</sup>

**ABSTRACT:** The performance of an interface elastoplastic constitutive model for the analysis of unreinforced masonry structures is evaluated. Both masonry components are discretized aiming at a rational unit-joint model able to describe cracking, slip, and crushing of the material. The model is formulated in the spirit of softening plasticity for tension, shear and compression, with consistent treatment of the intersections defined by these modes. The numerical implementation is based on modern algorithmic concepts such as local and global Newton-Raphson methods, implicit integration of the rate equations and consistent tangent stiffness matrices. The parameters necessary to define the model are derived from microexperiments in units, joints, and small masonry samples. The model is used to analyze masonry shear-walls and is capable of predicting the experimental collapse load and behaviour accurately. Detailed comparisons between experimental and numerical results permit a clear understanding of the walls structural behavior, flow of internal forces and redistribution of stresses both in the pre- and post-peak regime.

## INTRODUCTION

Masonry is a composite material made of units, e.g., clay bricks or concrete blocks, and mortar. The large number of influence factors, such as anisotropy of units, dimension of units, joint width, material properties of the units and mortar, arrangement of bed as well as head joints and quality of workmanship, make the simulation of masonry structures extremely difficult. Moreover, an accurate masonry description needs a complete set of experimental data.

Recently, the masonry research community began to show interest in sophisticated numerical models as an opposition to the prevailing tradition of rules of thumb or empirical formulae. These were, in general, acquired with years of practice and experimental testing. The present article follows naturally from a rational attempt to achieve a more fundamental insight in the behavior of masonry and to permit more competitive use of masonry. Here, attention will be given to micromodels, wherein the two masonry components are modelled separately. Interface elements are used as potential crack, slip, or crushing planes. A new interface cap model, recently developed by the writers see Lourenço et al. (1994), in modern plasticity concepts, is able to capture all masonry failure mechanisms. The model includes a tension cut-off for Mode I failure, a Coulomb friction envelope for Mode II failure and a cap model for compressive failure. In addition, interface elements are considered to model potential cracks in the units. The implementation of the model is briefly reviewed here and includes proper handling of the nonsmooth corners, use of a local Newton-Raphson to solve the implicit Euler backward return mapping and consistent tangent moduli. Such set of procedures leads to a robust and accurate numerical algorithm that preserves quadratic convergence. The parameters necessary to define the model are derived from carefully displacement controlled microexperiments. The main difference between the present strategy and the research carried out by other authors, see Lourenço and Rots (1993) for references and Lofti and Shing (1994), lies in the assumption that all the inelastic phenomena

occur in the interface elements. This assumption leads to a robust type of modelling, capable of following the complete load path of a structure until total degradation of stiffness. To the knowledge of the authors most previous numerical microanalyses (and also most of the experimental results) are limited to the structural prepeak regime. Computations beyond the limit load down to a possibly lower residual load are, however, needed to assess the safety of the structure.

## CAP MODEL FOR MASONRY

An accurate model for masonry has to include the basic types of mechanisms that characterize the material: (a) Cracking in the joints; (b) sliding along a bed or head joint at low values of normal stress; (c) cracking of the masonry units in direct tension; (d) diagonal tension cracking of masonry units at values of normal stress sufficient to develop friction in joints; and (e) splitting of units in tension as a result of mortar dilatancy at high values of normal stress (see Fig. 1). It is

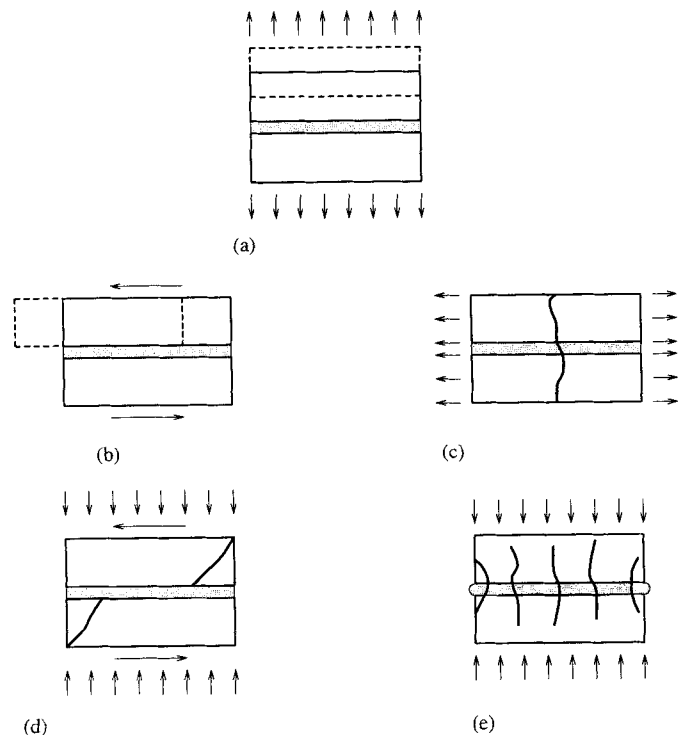


FIG. 1. Failure Mechanisms of Masonry: (a) Joint Tension Cracking; (b) Joint Slip; (c) Unit Direct Tension Crack; (d) Unit Diagonal Tension Crack; (e) Masonry Crushing

<sup>1</sup>Res. Engr., Delft Univ. of Technol. Fac. of Civ. Engrg., Delft, The Netherlands; presently at Dept. of Civ. Engrg., School of Engrg., Univ. of Minho, Azurém, 4800 Guimarães, Portugal.

<sup>2</sup>Sr. Res. Fellow, Delft Univ. of Technol./TNO Build. and Constr. Res., P.O. Box 49, 2600 AA Delft, The Netherlands.

Note. Associate Editor: Robert Y. Liang. Discussion open until December 1, 1997. To extend the closing date one month, a written request must be filed with the ASCE Manager of Journals. The manuscript for this paper was submitted for review and possible publication on March 24, 1995. This paper is part of the *Journal of Engineering Mechanics*, Vol. 123, No. 7, July, 1997. ©ASCE, ISSN 0733-9399/97/0007-0660-0668/\$4.00 + \$.50 per page. Paper No. 10403.

clear from the described phenomena that (a, b) are joint mechanisms, (c) is a brick mechanism and (d, e) are combined mechanisms involving bricks and joints. Attempts to use interfaces for the modelling of masonry were carried out in the last decade with reasonably simple models and without including all the above mechanisms, see Lourenço and Rots (1993) for references.

The question remains of how to consider all phenomena in the model. The approach followed here is to concentrate all the damage in the relatively weak joints and, if necessary, in potential pure tension cracks in the units placed vertically in the middle of each unit (see Fig. 2). The joint interface yield surface has then to include all the mechanisms referred above except uniaxial tensile cracking of the unit. Inclusion of the first two mechanisms (tensile and shear failure of the joint) has been pursued before but the cap model here set forth is novel. By limiting the compression/shear stress combinations the compressive damage can be included in the model as well as the combined mortar shear failure and unit diagonal tension failure. The new interface cap model to be developed is used at a micro-level. Remarkably, experiments carried out on, e.g., shear-walls (Mann and Müller 1982) result in similar macro-level yield surfaces (see Fig. 3).

The formulation of isoparametric interface elements has evolved rather far and the reader is referred to Hohberg (1992) for an exhaustive discussion. One of the most important issues is the selection of an appropriate integration scheme, e.g., a

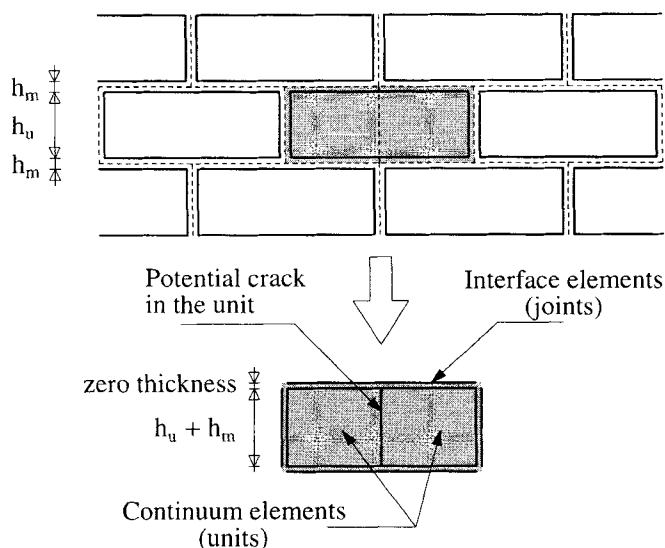


FIG. 2. Suggested Modeling Strategy [Units ( $u$ ), Which Are Expanded in Both Directions by Mortar Thickness, Are Modeled with Continuum Elements; Mortar Joints ( $m$ ) and Potential Cracks in Units Are Modeled with Zero-Thickness Interface Elements]

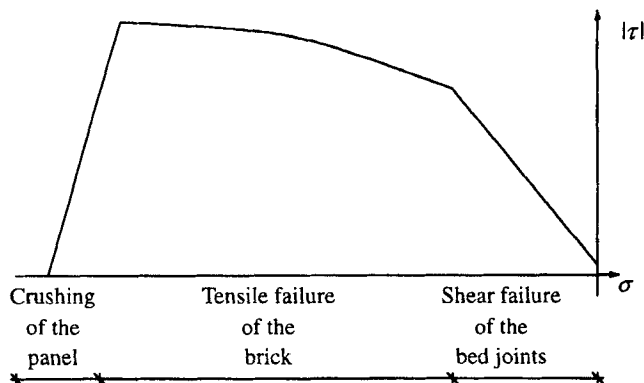


FIG. 3. Failure Surface for Shear Walls (Mann and Müller 1982)

lumped or Lobatto scheme, as Gauss integration was reported to lead to oscillations of stresses when high stiffnesses are used, see Rots (1988). An interface element allows discontinuities in the displacement field and its behaviour is described in terms of a relation between the tractions  $\mathbf{t}$  and relative displacements  $\mathbf{u}$  across the interface. In the present paper such quantities will be denoted as  $\boldsymbol{\sigma}$ , generalized stress, and  $\boldsymbol{\epsilon}$ , generalized strain. In this case the elastic constitutive relation between stresses and strains is given as usual by

$$\boldsymbol{\sigma} = \mathbf{D}\boldsymbol{\epsilon} \quad (1)$$

For a 2D configuration  $\mathbf{D} = \text{diag}\{k_n, k_s\}$ ,  $\boldsymbol{\sigma} = (\sigma, \tau)^T$  and  $\boldsymbol{\epsilon} = (u_n, u_s)^T$ , where  $n$  and  $s$  = normal and shear components, respectively. The terms in the elastic stiffness matrix can be obtained from the properties of both masonry components and the thickness of the joint as

$$k_n = \frac{E_u E_m}{t_m(E_u + E_m)}; \quad k_s = \frac{G_u G_m}{t_m(G_u + G_m)} \quad (2)$$

where  $E_u$  and  $E_m$  = Young's moduli;  $G_u$  and  $G_m$  = shear moduli, respectively, for unit and mortar; and  $t_m$  = thickness of joint. The stiffness values obtained from these formulae do not correspond to a penalty approach, which means that overlap of neighboring units subjected to compression will become visible already in the elastic regime. This feature is, however, intrinsic to the interface elements formulation and is independent from the values of normal stiffness, even if it is clear that the amount of penetration will be higher with decreasing interface stiffness. The interface model includes a compressive cap where the complete inelastic behaviour of masonry in compression is lumped. This is a phenomenological representation of masonry crushing because the failure process in compression is, in reality, explained by the microstructure of units and mortar and the interaction between them. In the model the failure mechanism is represented in such a way that the global stress-displacement diagram is captured and corresponds to one unit literally imploding over the other. As can be gathered from some confusing statements in the literature, it takes some time to get used to this zero or "negative" volume (in compressed state) of interface elements (Hohberg 1992).

## MULTISURFACE PLASTICITY

The elastic domain is bounded by a composite yield surface that includes tension, shear and compression failure with softening (see Fig. 4). For the implementation of this model single surface and multisurface plasticity theory is reviewed below in modern concepts, including consistent tangent operators and correct handling of the corners.

For multisurface plasticity the form of the elastic domain is defined by each yield function  $f_i < 0$ . Loading/unloading can be conveniently established in standard Kuhn-Tucker form by means of the conditions

$$\dot{\lambda}_i \geq 0, f_i \leq 0 \quad \text{and} \quad \dot{\lambda}_i f_i = 0 \quad (3)$$

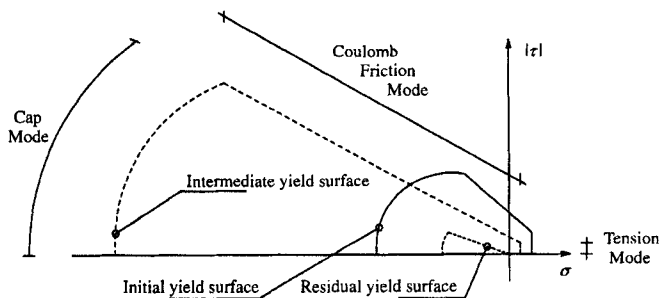


FIG. 4. Proposed Interface Cap Model

where  $\dot{\lambda}_i$  = plastic multiplier rate. Here it will be assumed that the yield functions are of the form

$$f_i(\boldsymbol{\sigma}, \kappa_i) = \Phi_i(\boldsymbol{\sigma}) + \Psi_i(\kappa_i) \quad (4)$$

where scalar  $\kappa_i$  = amount of hardening or softening; and  $\Phi_i$ ,  $\Psi_i$  = generic functions. The usual elastoplastic equations for single surface plasticity hold: the total strain rate  $\dot{\boldsymbol{\epsilon}}$  is decomposed into an elastic component  $\dot{\boldsymbol{\epsilon}}^e$  and a plastic component  $\dot{\boldsymbol{\epsilon}}^p$

$$\dot{\boldsymbol{\epsilon}} = \dot{\boldsymbol{\epsilon}}^e + \dot{\boldsymbol{\epsilon}}^p \quad (5)$$

the elastic strain rate is related to the stress rate by the elastic constitutive matrix  $\mathbf{D}$  as

$$\dot{\boldsymbol{\sigma}} = \mathbf{D}\dot{\boldsymbol{\epsilon}}^e \quad (6)$$

and the assumption of nonassociated plasticity yields

$$\dot{\boldsymbol{\epsilon}}^p = \dot{\lambda} \frac{\partial g}{\partial \boldsymbol{\sigma}} \quad (7)$$

where  $g$  = plastic potential. The scalar  $\kappa$  introduced before reads, in case of strain hardening/softening

$$\dot{\kappa} = \sqrt{(\dot{\boldsymbol{\epsilon}}^p)^T \dot{\boldsymbol{\epsilon}}^p} \quad (8)$$

For any corner of the proposed model two yield surfaces are active and the previous equations must be appropriately stated for multisurface plasticity. According to Koiter's generalization (Koiter 1953), (7) reads

$$\dot{\boldsymbol{\epsilon}}^p = \dot{\boldsymbol{\epsilon}}_1^p + \dot{\boldsymbol{\epsilon}}_2^p = \dot{\lambda}_1 \frac{\partial g_1}{\partial \boldsymbol{\sigma}} + \dot{\lambda}_2 \frac{\partial g_2}{\partial \boldsymbol{\sigma}} \quad (9)$$

and, assuming a form of explicit coupling for the hardening/softening parameters, we obtain

$$\dot{\kappa}_1^{\text{corner}} = \dot{\kappa}_1 + \zeta_{12}\dot{\kappa}_2 \quad \text{and} \quad \dot{\kappa}_2^{\text{corner}} = \zeta_{21}\dot{\kappa}_1 + \dot{\kappa}_2 \quad (10)$$

where  $\zeta_{12}$  and  $\zeta_{21}$  are coupling terms.

### Integration of Elastoplastic Equations

The return mapping algorithm is strain driven and basically consists of two steps, the calculation of the elastic trial stress, also called the elastic predictor, and the return mapping to the yield surface, i.e., the plastic corrector. We will use the implicit Euler backward integration scheme due to its unconditional stability (Ortiz and Popov 1985) and accuracy (de Borst and Feenstra 1990). For single surface plasticity, manipulation of (5)–(7) for finite increments and application of an implicit Euler backward integration scheme gives the update of the stress values as

$$\boldsymbol{\sigma}_{n+1} = \boldsymbol{\sigma}_n + \Delta\boldsymbol{\sigma}_{n+1} = \boldsymbol{\sigma}_n + \mathbf{D}\Delta\boldsymbol{\epsilon}_{n+1}^e = \boldsymbol{\sigma}_n + \mathbf{D}(\Delta\boldsymbol{\epsilon}_{n+1} - \Delta\boldsymbol{\epsilon}_{n+1}^p) \quad (11)$$

This equation can be recast as

$$\boldsymbol{\sigma}_{n+1} = \boldsymbol{\sigma}_{n+1}^{\text{trial}} - \Delta\lambda_{n+1}\mathbf{D} \frac{\partial g}{\partial \boldsymbol{\sigma}} \bigg|_{n+1} \quad (12)$$

with  $\boldsymbol{\sigma}_{n+1}^{\text{trial}} = \boldsymbol{\sigma}_n + \mathbf{D}\Delta\boldsymbol{\epsilon}_{n+1}$ . The subscript  $n+1$  means that all the quantities are evaluated at the final stage. For simplicity it will be, in general, dropped in the derivatives. (12) represents a nonlinear system of equations with the stress tensor components and one scalar (usually  $\Delta\lambda_{n+1}$ ) as unknowns. Enforcing the satisfaction of the yield condition at the final converged stage results in the necessary additional equation

$$f_{n+1} = 0 \quad (13)$$

The constitutive nonlinear equations [(12) and (13)] at the integration point level can be solved locally with a regular New-

ton-Raphson method. In most cases, and for the yield functions used in the present paper, (12) can be solved in order to obtain explicitly the updated stress value as a function of the updated plastic multiplier

$$\boldsymbol{\sigma}_{n+1} = \boldsymbol{\sigma}_{n+1}(\Delta\lambda_{n+1}) \quad (14)$$

Furthermore, inserting (7) in (8) yields for finite increments

$$\Delta\kappa_{n+1} = \Delta\kappa_{n+1}(\boldsymbol{\sigma}_{n+1}, \Delta\lambda_{n+1}) \quad (15)$$

Substitution of these two equations in the yield function, cf. (13), leads to a nonlinear equation in one variable, namely  $\Delta\lambda_{n+1}$ :  $f_{n+1}(\Delta\lambda_{n+1}) = 0$ . This constitutive equation is solved here with a local Newton method. The derivative of  $f_{n+1}(\Delta\lambda_{n+1})$  with respect to  $\Delta\lambda_{n+1}$ , which is needed in this procedure, reads after some manipulation

$$\frac{\partial f}{\partial \Delta\lambda} \bigg|_{n+1} = \boldsymbol{\gamma}^T \frac{\partial \boldsymbol{\sigma}}{\partial \Delta\lambda} - h \quad (16)$$

where the modified yield surface gradient  $\boldsymbol{\gamma}$  and the hardening modulus  $h$  are given by

$$\boldsymbol{\gamma} = \frac{\partial f}{\partial \boldsymbol{\sigma}} + \frac{\partial f}{\partial \kappa} \frac{\partial \kappa}{\partial \boldsymbol{\sigma}} \bigg|_{n+1} \quad \text{and} \quad h = -\frac{\partial f}{\partial \kappa} \frac{\partial \kappa}{\partial \Delta\lambda} \bigg|_{n+1} \quad (17)$$

For multisurface plasticity a similar procedure applies and (12) reads now

$$\boldsymbol{\sigma}_{n+1} = \boldsymbol{\sigma}_{n+1}^{\text{trial}} - \Delta\lambda_{1,n+1}\mathbf{D} \frac{\partial g_1}{\partial \boldsymbol{\sigma}} \bigg|_{n+1} - \Delta\lambda_{2,n+1}\mathbf{D} \frac{\partial g_2}{\partial \boldsymbol{\sigma}} \bigg|_{n+1} \quad (18)$$

We shall equally assume that this equation can be solved explicitly as

$$\boldsymbol{\sigma}_{n+1} = \boldsymbol{\sigma}_{n+1}(\Delta\lambda_{1,n+1}, \Delta\lambda_{2,n+1}) \quad (19)$$

As for single surface plasticity, (10) yields for finite increments

$$\begin{aligned} \kappa_{1,n+1}^{\text{corner}} &= \kappa_{1,n+1}^{\text{corner}}(\boldsymbol{\sigma}_{n+1}, \Delta\lambda_{1,n+1}, \Delta\lambda_{2,n+1}); \quad \kappa_{2,n+1}^{\text{corner}} \\ &= \kappa_{2,n+1}^{\text{corner}}(\boldsymbol{\sigma}_{n+1}, \Delta\lambda_{1,n+1}, \Delta\lambda_{2,n+1}) \end{aligned} \quad (20)$$

Substitution of these two equations in the active yield functions leads to a nonlinear system of equations with a set of scalar unknowns, namely  $\Delta\lambda_{1,n+1}$  and  $\Delta\lambda_{2,n+1}$

$$f_{1,n+1}(\Delta\lambda_{1,n+1}, \Delta\lambda_{2,n+1}) = 0; \quad f_{2,n+1}(\Delta\lambda_{1,n+1}, \Delta\lambda_{2,n+1}) = 0 \quad (21)$$

This nonlinear constitutive system of equations is solved by a local Newton-Raphson iterative method. The Jacobian necessary for the Newton-Raphson scheme reads

$$\mathbf{J}_{n+1} = \begin{bmatrix} \boldsymbol{\gamma}_1^T \frac{\partial \boldsymbol{\sigma}}{\partial \Delta\lambda_1} - h_1 & \boldsymbol{\gamma}_1^T \frac{\partial \boldsymbol{\sigma}}{\partial \Delta\lambda_2} + \frac{\partial f_1}{\partial \kappa_1} \frac{\partial \kappa_1}{\partial \Delta\lambda_2} \\ \boldsymbol{\gamma}_2^T \frac{\partial \boldsymbol{\sigma}}{\partial \Delta\lambda_1} + \frac{\partial f_2}{\partial \kappa_2} \frac{\partial \kappa_2}{\partial \Delta\lambda_1} & \boldsymbol{\gamma}_2^T \frac{\partial \boldsymbol{\sigma}}{\partial \Delta\lambda_2} - h_2 \end{bmatrix} \quad (22)$$

where

$$\boldsymbol{\gamma}_i = \frac{\partial f_i}{\partial \boldsymbol{\sigma}} + \frac{\partial f_i}{\partial \kappa_i} \frac{\partial \kappa_i}{\partial \boldsymbol{\sigma}} \bigg|_{n+1} \quad \text{and} \quad h_i = -\frac{\partial f_i}{\partial \kappa_i} \frac{\partial \kappa_i}{\partial \Delta\lambda_i} \bigg|_{n+1} \quad (23)$$

The problem that remains is how to determine the set of active yield functions, see Simo et al. (1988). In the present article a trial-and-error procedure to solve the return mapping is used. It will be assumed that the set of initial active yield functions is the one defined by Simo et al. (1988) ( $f_i^{\text{trial}} \geq 0$ ). If, after the return mapping is completed, any  $\Delta\lambda_{i,n+1}^i < 0$  or  $f_{i,n+1}^i > 0$  is found, the number of active yield surfaces is adjusted accordingly and the return mapping is restarted. During

this process one restart may be required, or, rarely and only for larger increments, more restarts may be required before the correct number of active yield surfaces is obtained.

### Evaluation of Tangent Operator

A tangent operator consistent with the integration algorithm is needed to obtain quadratic convergence and a robust global Newton-Raphson method. For single surface plasticity, differentiation of the update equations [(12) and (15)] and the consistency condition ( $df_{n+1} = 0$ ) yield after algebraic manipulation the consistent tangent operator  $\mathbf{D}^{ep}$  as, see Lourenço et al. (1994)

$$\mathbf{D}^{ep} = \frac{d\boldsymbol{\sigma}}{d\boldsymbol{\epsilon}} \bigg|_{n+1} = \mathbf{H}^{-1} - \frac{\mathbf{H}^{-1} \frac{\partial g}{\partial \boldsymbol{\sigma}} \boldsymbol{\gamma}^T \mathbf{H}^{-1}}{h + \boldsymbol{\gamma}^T \mathbf{H}^{-1} \frac{\partial g}{\partial \boldsymbol{\sigma}}} \quad (24)$$

where the modified compliance matrix  $\mathbf{H}$  is given by

$$\mathbf{H} = \mathbf{D}^{-1} + \Delta\lambda_{n+1} \frac{\partial^2 g}{\partial \boldsymbol{\sigma}^2} \quad (25)$$

The above expression for  $\mathbf{D}^{ep}$  is particularly interesting as it clearly shows that a nonsymmetric tangent operator will be obtained even in the case of associated plasticity if the hardening parameter update is not a linear function of the plastic multiplier update, i.e., if  $\Delta\kappa_{n+1} \neq c\Delta\lambda_{n+1}$ , where  $c$  is a constant.

Similarly, for multisurface plasticity, differentiation of the update equations [(18) and (20)] and the consistent conditions ( $df_{1,n+1} = 0$  and  $df_{2,n+1} = 0$ ) yield after algebraic manipulation the consistent tangent operator  $\mathbf{D}^{ep}$  as, see Lourenço et al. (1994)

$$\mathbf{D}^{ep} = \frac{d\boldsymbol{\sigma}}{d\boldsymbol{\epsilon}} \bigg|_{n+1} = \mathbf{H}^{-1} - \mathbf{H}^{-1} \mathbf{U} (\mathbf{E} + \mathbf{V}^T \mathbf{H}^{-1} \mathbf{U})^{-1} \mathbf{V}^T \mathbf{H}^{-1} \quad (26)$$

where the modified compliance matrix  $\mathbf{H}$  reads now

$$\mathbf{H} = \mathbf{D}^{-1} + \Delta\lambda_{1,n+1} \frac{\partial^2 g_1}{\partial \boldsymbol{\sigma}^2} + \Delta\lambda_{2,n+1} \frac{\partial^2 g_2}{\partial \boldsymbol{\sigma}^2} \quad (27)$$

the matrix  $\mathbf{U}$  reads

$$\mathbf{U} = \begin{bmatrix} \frac{\partial g_1}{\partial \boldsymbol{\sigma}} & \frac{\partial g_2}{\partial \boldsymbol{\sigma}} \end{bmatrix} \quad (28)$$

the matrix  $\mathbf{V}$  reads

$$\mathbf{V} = [\boldsymbol{\gamma}_1 \quad \boldsymbol{\gamma}_2] \quad (29)$$

and the matrix  $\mathbf{E}$  reads

$$\mathbf{E} = \begin{bmatrix} -h_1 & \frac{\partial f_1}{\partial \kappa_1} \frac{\partial \Delta\lambda_1}{\partial \lambda_1} \\ \frac{\partial f_2}{\partial \kappa_2} \frac{\partial \Delta\lambda_2}{\partial \lambda_2} & -h_2 \end{bmatrix} + \begin{bmatrix} \frac{\partial f_1}{\partial \kappa_1} \frac{\partial \Delta\lambda_2}{\partial \lambda_2} & 0 \\ 0 & \frac{\partial f_2}{\partial \kappa_2} \frac{\partial \Delta\lambda_1}{\partial \lambda_1} \end{bmatrix} \quad (30)$$

### FORMULATION OF MODEL

Cap models originated in the field of soil mechanics. The introduction of a spherical cap for the Drucker-Prager model was firstly made by Drucker et al. (1957) to describe plastic compaction and to enhance the behaviour in hydrostatic compression. Since then various models were suggested, e.g., the well-known Cam-clay model (Roscoe and Burland 1968). Recently the numerical algorithm has been revised by Hofstetter et al. (1993) with the use of unconditionally stable closest point projection return mappings, tangent operators consistent with the integration algorithm and proper handling of the corners. Previous cap models have been, in general, limited to

associated plasticity and hardening/softening of the cap while the other yield surfaces remain in ideal plasticity.

For the application envisaged here the behavior found experimentally leads to a more complex model. Most masonry joints have extremely low dilatancy and the model must be formulated in the context of nonassociated plasticity. Also softening behavior should be included for all modes of the composite yield surface. The model presented in this article is of general application but the formulation is shown in the characteristic interface ( $\sigma$ ,  $\tau$ )-space. The reader can assume the usual ( $I_1$ ,  $\sqrt{J_2}$ )-space formulation for regular continuum elements.

### Tension Mode

For the tension mode, exponential softening on the tensile strength is assumed according to the mode I experiments by van der Pluijm (1992) (see Fig. 5). In this figure, the shaded area represents the envelope of three tests. The yield function reads

$$f_t(\boldsymbol{\sigma}, \kappa_1) = \sigma - f_t(\kappa_1) \quad (31)$$

where the yield value  $f_t$  reads

$$f_t = f_{t0} \exp \left( -\frac{f_{t0}}{G_f^I} \kappa_1 \right) \quad (32)$$

where  $f_{t0}$  = tensile strength of joint or, more precisely, of unit-mortar interface (which is the weakest link); and  $G_f^I$  = mode I fracture energy. An associated flow and a strain softening hypothesis are considered. Assuming that only the normal plastic relative displacement controls the softening behavior, (8) yields

$$\dot{\kappa}_1 = |\dot{u}_n^p| = \dot{\lambda}_1 \quad (33)$$

### Shear Mode

For the Coulomb friction mode, the yield function reads

$$f_s(\boldsymbol{\sigma}, \kappa_2) = |\tau| + \sigma \tan \phi(\kappa_2) - c(\kappa_2) \quad (34)$$

Based on microshear experiments by van der Pluijm (1993), the yield values  $c$  and  $\tan \phi$  are assumed

$$c = c_0 \exp \left( -\frac{c_0}{G_f^II} \kappa_2 \right) \quad (35)$$

and

$$\tan \phi = \tan \phi_0 + (\tan \phi_r - \tan \phi_0) \frac{c_0 - c}{c_0} \quad (36)$$

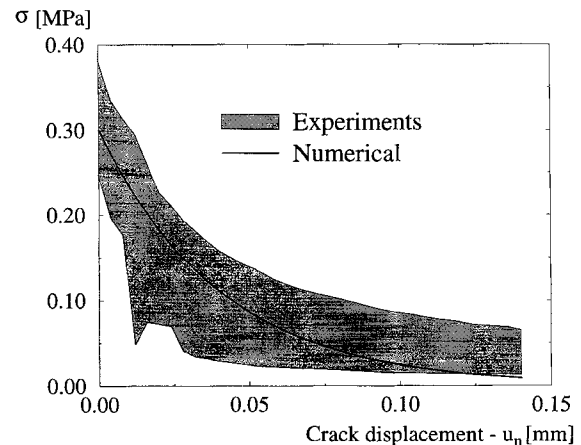


FIG. 5. Tensile Behavior of Present Model versus Experimental Results from van der Pluijm (1992) ( $f_t = 0.30$  MPa;  $G_f^I = 0.012$  N/mm)

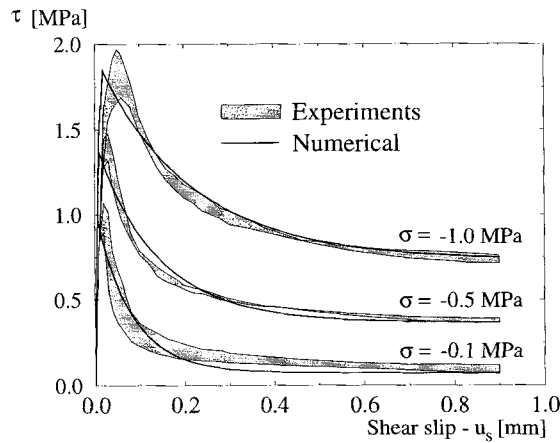


FIG. 6. Shear Behavior of Present Model versus Experimental Results by van der Pluijm (1993) for Different Confinement Levels [ $c_0 = 0.87$  MPa;  $\tan \phi_0 = 1.01$ ;  $\tan \phi_r = 0.73$ ;  $G_f'' = 0.058 - 0.13\sigma$  (N/mm)]

where  $c_0$  = initial cohesion of joint;  $\tan \phi_0$  = initial friction angle;  $\tan \phi_r$  = residual friction angle; and  $G_f''$  = mode II fracture energy. Note that exponential softening is assumed for the cohesion (see Fig. 6) and that, for simplicity, the softening of the friction angle is taken proportional to the softening of the cohesion. A nonassociated plastic potential  $g_2$

$$g_2 = |\tau| + \sigma \tan \psi - c \quad (37)$$

where a dilatancy angle  $\psi$  and a strain softening hypothesis are considered. In the computational implementation of the model, the dilatancy angle is considered as a function of the plastic relative shear displacement and the normal confining pressure. Under increasing values of these two quantities, the dilatancy angle tends to zero. This is physically realistic due to the micro granular structure of mortar and is also confirmed in the experiments, see van der Pluijm (1993). Assuming that only the shear plastic relative displacement controls the softening behavior, (8) yields

$$\dot{\kappa}_2 = |\dot{u}_s^p| = \dot{\lambda}_2 \quad (38)$$

### Permanent Coupling of Tension/Shear Mode

The tension and Coulomb friction modes are coupled with isotropic softening. This means that the percentage of softening on the cohesion is assumed to be the same as on the tensile strength and, for exponential softening, (33) and (38) must be rewritten as

$$\dot{\kappa}_1 = \dot{\lambda}_1 + \frac{G_f'}{G_f''} \frac{c_0}{f_{t0}} \dot{\lambda}_2; \quad \dot{\kappa}_2 = \frac{G_f''}{G_f'} \frac{f_{t0}}{c_0} \dot{\lambda}_1 + \dot{\lambda}_2 \quad (39)$$

These relations can be directly obtained from (32) and (35). It is noted that (39) according to Kuhn-Tucker conditions, cf. (3), indicate that the shear and tension modes represent, in reality, only one discontinuous yield surface and not two. The two scalars shown as a measure of softening,  $\kappa_1$  and  $\kappa_2$ , represent a single scalar. In the computational code however, the measure of shear softening and tensile softening are updated independently to posterior check which type of softening has occurred. During postprocessing of the results, this is relevant for a good understanding of the structural behaviour.

### Cap Mode

For the cap mode, an ellipsoid interface model is used. The yield condition is now given by

$$f_3(\sigma, \kappa_3) = C_{nn}\sigma^2 + C_{ss}\tau^2 + C_n\sigma - \bar{\sigma}^2(\kappa_3) \quad (40)$$

where  $C_{nn}$ ,  $C_{ss}$ , and  $C_n$  = set of material parameters; and  $\bar{\sigma}$  = yield value. For the hardening/softening behavior the law shown in Fig. 7 was considered. Note that the curved diagram leads to a  $C^1$  continuous  $\sigma - \epsilon$  relationship (see Fig. 8). The approach shown in Fig. 7 can be used for interface elements because a direct relation between stresses and displacements is established. The energy under the curve can be related to a "compressive fracture energy."

Using matrix notation, (40) can be rewritten as

$$f_3(\sigma, \kappa_3) = 1/2\sigma^T \mathbf{P} \sigma + p^T \sigma - \bar{\sigma}^2(\kappa_3) \quad (41)$$

where  $\mathbf{P} = \text{diag} \{2C_{nn}, 2C_{ss}\}$  and  $\mathbf{p} = (C_n, 0)^T$ .

An associated flow and a strain hardening/softening hypothesis are considered. This yields, upon substitution in (8)

$$\dot{\kappa}_3 = \dot{\lambda}_3 \sqrt{(\mathbf{P}\sigma + \mathbf{p})^T (\mathbf{P}\sigma + \mathbf{p})} \quad (42)$$

### Corners

The theory for multisurface plasticity is described in the previous section. Only additional remarks about the corners will be detailed here.

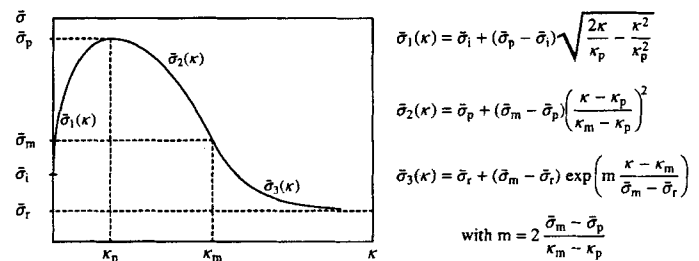


FIG. 7. Hardening/Softening Law for Cap Mode

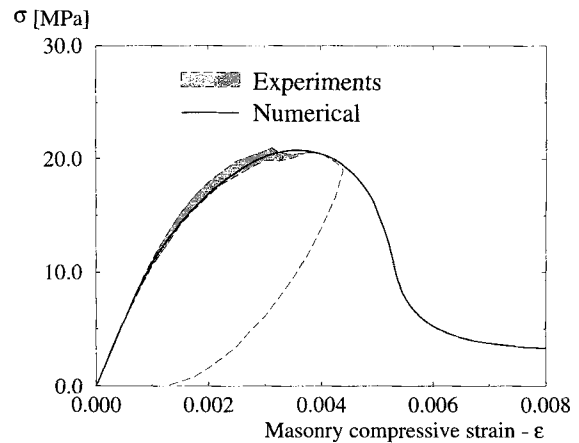


FIG. 8. Model versus Experimental Compressive Behavior [Compressive Strength = 20.8 MPa; Inelastic Parameters from Atkinson and Yan (1990)]

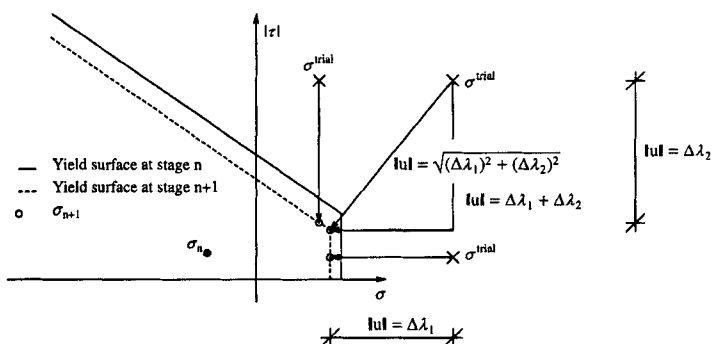


FIG. 9. Softening of Tension/Shear Mode

For the tension/shear corner (39) yields a stronger penalization than adjacent single surface modes as shown in Fig. 9. This figure shows three different possible trial stress states close to the corner and the respective return mapping. It is further assumed that the yield surface at stage  $n + 1$  is the same for the three cases (this is clearly wrong but yields a more legible picture), the stiffness matrix is equal to the identity matrix and the dilatancy equals zero. Then, for the shear and tension modes, the amount of softening is measured by the distance  $\Delta\lambda_{i,n+1} = |\sigma^{\text{trial}} - \sigma_{n+1}|$ . In the corner, according to (39), the two values will be added representing a nonacceptable penalty. For this reason a quadratic combination is assumed, reading

$$\kappa_1 = \sqrt{(\dot{\lambda}_1)^2 + \left(\frac{G_f' c_0}{G_f'' f_0} \dot{\lambda}_2\right)^2}; \quad \kappa_2 = \sqrt{\left(\frac{G_f'' f_0}{G_f' c_0} \dot{\lambda}_1\right)^2 + (\dot{\lambda}_2)^2} \quad (43)$$

Note that these equations yield additional terms for the Jacobian used for the local Newton-Raphson method, cf., (22). For the shear/cap corner the yield surfaces are assumed to be uncoupled.

## NUMERICAL EXAMPLES

Tests on masonry shear walls were carried out by Raijmakers and Vermeltoort (1992) and Vermeltoort and Raijmakers (1993). Two types of walls were considered, either with an opening in the center, hereby designated by "hollow wall," or a complete panel, hereby designated by "solid wall." These tests are particularly suitable for the appraisal of the model

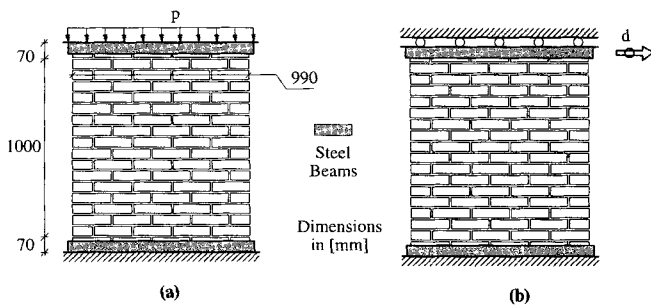


FIG. 10. Loads for Hollow and Solid Shear Walls: (a) Phase 1—Vertical Loading; (b) Phase 2—Horizontal Loading

TABLE 1. Properties for Potential Brick Cracks

$k_n$ (1)	$k_s$ (2)	$f_0$ (3)	$G_f'$ (4)
$1.0 \times 10^6$ N/mm <sup>3</sup>	$1.0 \times 10^6$ N/mm <sup>3</sup>	2.0 N/mm <sup>2</sup>	0.08 N/mm

TABLE 2. Elastic Properties for Bricks and Joints

Brick		Joint	
$E$ (1)	$\nu$ (2)	$k_n$ (3)	$k_s$ (4)
16,700 N/mm <sup>2</sup>	0.15 —	82; 110; 82 N/mm <sup>3</sup>	36; 50; 36 N/mm <sup>3</sup>

TABLE 3. Inelastic Properties for Joints

Tension		Shear					Cap			
$f_0$ (1)	$G_f'$ (2)	$c_0$ (3)	$\tan \phi_0$ (4)	$\tan \phi_r$ (5)	$\tan \psi$ (6)	$G_f''$ (7)	$f_m$ (8)	$C_{nn}$ (9)	$C_{ss}$ (10)	$C_n$ (11)
0.25; 0.16; 0.16 N/mm <sup>2</sup>	0.018 N/mm	$1.4 f_0$ N/mm <sup>2</sup>	0.75 —	0.75 —	0.0 —	0.125; 0.050; 0.050 N/mm	10.5; 11.5; 11.5 N/mm <sup>2</sup>	1.0 —	9.0 —	0.0 N/mm <sup>2</sup>

performance as quite comprehensive experimental data was recorded. Moreover, the parameters necessary to characterize the material model are available from companion microexperiments.

The specimen consists of a pier with a width/height ratio of one ( $990 \times 1000$  mm<sup>2</sup>), built up with 18 courses (16 active courses and 2 courses clamped in steel beams) of Joosten solid clay bricks (dimensions  $204 \times 98 \times 50$  mm<sup>3</sup>) and 10-mm-thick mortar (1:2:9, cement:lime:sand by volume). The piers were subjected to a vertical uniformly distributed load  $p$  before a horizontal load was monotonically increased under top displacement control  $d$  until failure (see Fig. 10).

For the numerical analyses, bricks are represented by plane stress continuum elements (8-noded) while line interface elements (6-noded) are adopted for joints and, if necessary, for the potential vertical cracks in the middle of the brick. Each brick is modeled with  $4 \times 2$  elements. For the joints, the composite yield function described is adopted and, for the potential cracks in the bricks, a simple Mode I cracking model with exponential tensile softening and immediate drop to zero of the shear stress after initiation of the crack is assumed. The material data are obtained from the micro tension, compression and shear tests given before and are given in Tables 1–3. When more than one value is given in the same column this means that different values are used for the walls with an initial vertical load  $p$  of, respectively, 0.30, 1.21, and 2.12 N/mm<sup>2</sup>, according to the microtests in samples obtained from each wall. The hardening/softening law for the cap is the same as defined for the hollow walls. The hardening/softening law for the cap mode is defined by the set  $\{\bar{\sigma}, \kappa\}_i = \{(f_m/3, 0.0); (f_m, 0.09); (f_m/2, 0.49); (f_m/7, +\infty)\}$ .

## Hollow Walls

Two tests were successfully carried out with an initial vertical load  $p$  of 0.30 N/mm<sup>2</sup>. An opening placed in the middle of the wall defines two small, relatively weak piers and forces the compressive strut to spread through both sides of the opening leading to the ultimate cracking patterns shown in Fig. 11.

For the numerical simulation potential cracks in the bricks are not modelled as the experimental results indicated, in general, no visible cracks. Microcracking is likely to occur but it was assumed irrelevant for this analysis.

The comparison between the numerical and experimental load-displacement diagrams is shown in Fig. 12. The results agree well. The calculated failure load is equal to the failure load of one of the tests whereas the other test features a collapse load 20% lower than the calculated value. A good impression about the behavior of the model is also obtained because the calculated softening stiffness of the structure agrees well with the softening stiffness of one of the tests. This indicates that the same failure mechanism is predicted. It is however recognized that the behavior obtained numerically is more brittle than the experimental observations.

Globally, the analysis captures well the experimental behaviour of the walls, as illustrated in Fig. 13 (compare with Fig. 11). In this figure the word "damage" is used for the equivalent plastic strain of each mode of the cap model. Note that the cap "damage" is only shown in the softening range. Initially, two diagonal cracks arise from the corners of the open-

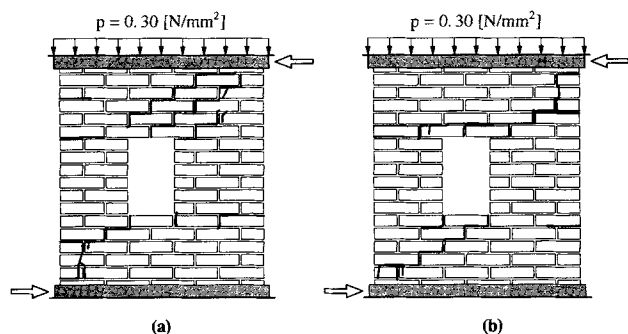


FIG. 11. Experimental Failure Patterns for Hollow Walls [Rajmakers (1992); Vermeltfoort (1993)]

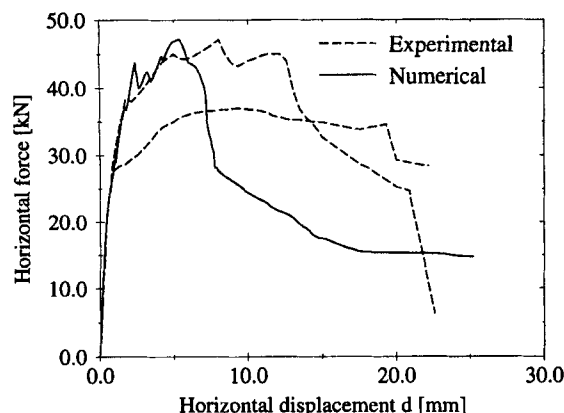


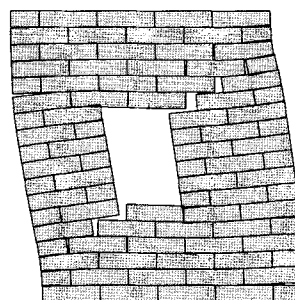
FIG. 12. Load-Displacement Diagrams for Hollow Wall

ing. These cracks are accompanied by less evident horizontal cracks in the top and bottom of the small piers as well as one horizontal crack in the bottom of the wall (see Fig. 13a). Under increasing deformation, the diagonal cracks that arose initially cannot progress to the compressed toes and two additional diagonal cracks start to open (see Fig. 13b). These become gradually predominant and, when the compressed toes at the bottom and top of the wall begin to crush, the previous diagonal cracks become inactive. Finally, a collapse mechanism is formed with the failure of the small piers in bending (crushing of the compressed toes and extended horizontal tension cracks) and the wall behaves similarly to four rigid blocks connected by the hinges shown in Fig. 13c.

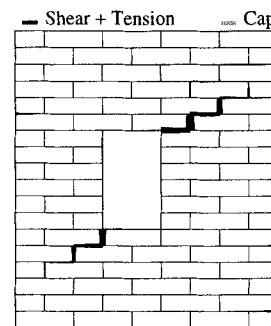
Remarkably it is possible to trace the complete path of the test without numerical difficulties. Full quadratic convergence was found during the entire prepeak and postpeak regimes. Note also that the snap throughs found in the numerical analysis are converged states due to the opening of new diagonal cracks and closing of previous diagonal cracks. These snaps were traced with arc-length control over opening, shearing or crushing of selected interfaces.

It is noted that, under the same loading conditions, the responses of the two tests, in terms of load-displacement diagrams, are different (see Fig. 12), and correspond to different crack patterns (see Fig. 11). It is believed that this is due to the combination of the scatter in the material properties and the small number of units that constitute the wall. It seems that different crack locations can be triggered for close failure loads, i.e., within the observed 20% range. The lower collapse load and more ductile behavior observed for one test correspond to an early sliding failure mode, involving the part of the wall above the opening, Fig. 11 (right). This is in opposition with the bending failure mode (with opening of the top-right corner) of the same part of the wall featured by the other test, Fig. 11 (left). A possible approach to reproduce an observed failure mode is to penalize or strengthen a certain num-

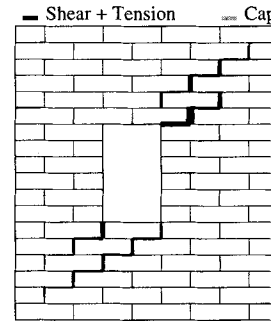
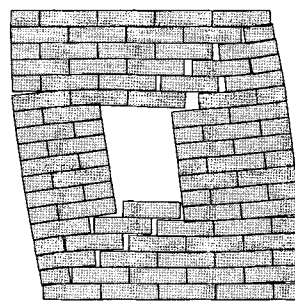
TOTAL DISPLACEMENTS



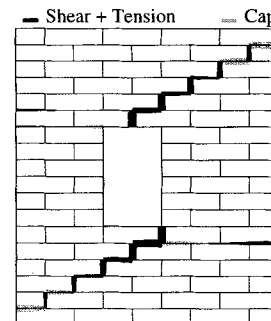
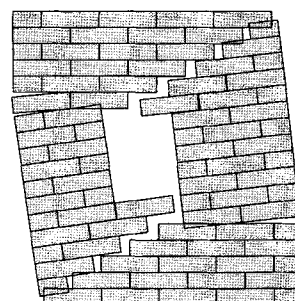
DAMAGE



(a)



(b)



(c)

FIG. 13. Numerical Results at Horizontal Displacement  $d$  (Hollow Walls): (a)  $d = 0.5$  mm; (b)  $d = 2.0$  mm; (c)  $d = 25.0$  mm

ber of joints in order to obtain exactly the crack pattern observed in a specific test but such inverse fitting is outside the scope of the present paper.

### Mesh Insensitivity

The mesh objectivity of the composite interface model is checked here by an additional numerical analysis in which each brick is modelled with  $8 \times 4$  elements. This leads to 4 times as many continuum elements and 2 times as many interface elements. As shown in Fig. 14, the results are almost identical, regarding the collapse load and the entire load-displacement diagram used to characterize the behavior of the structure. The interface cap model can be therefore considered to be mesh insensitive. This is another advantage of the interface approach when compared to crack band type models where mesh objectivity is a debated issue.

### Solid Walls

Tests were carried out for different initial vertical loads  $p$  of 0.30, 1.21 and 2.12 N/mm<sup>2</sup>. The crack patterns for the different walls tested are shown in Fig. 15. The behavior of the walls with a low initial vertical load is characterized by initial



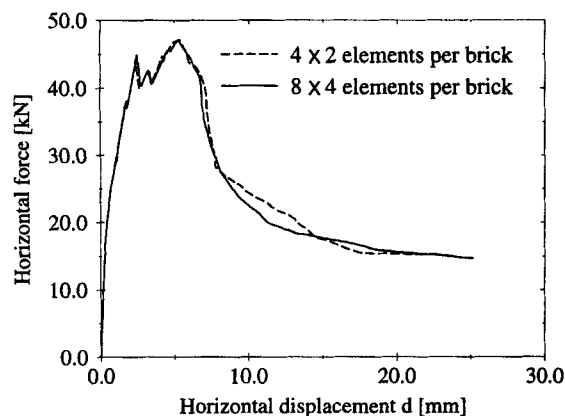


**FIG. 14. Load-Displacement Diagram for Two Different Mesh Discretizations**

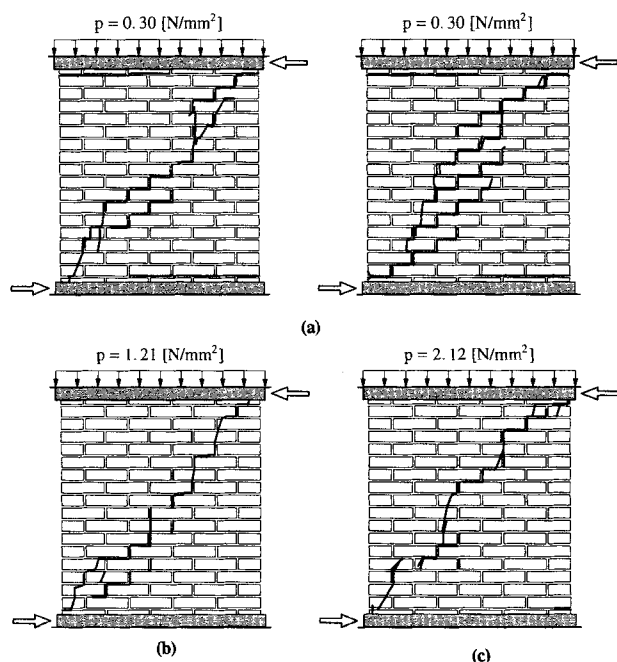


**FIG. 15. Experimental Failure Patterns for Solid Walls: (a)  $P = 30$  kN; (b)  $P = 120$  kN; (c)  $P = 210$  kN**

horizontal tension cracks that develop at the bottom and top of the wall. The collapse for all the walls is however characterized by a diagonal shear crack including cracks in the bricks and by crushing of the compressed toes.

From the failure patterns it is evident that cracks in the bricks need to be modeled. This is confirmed in Lourenço and Rots (1993). In that paper, the potential cracks in the bricks were not included, which led to an overestimation of the collapse load and a response much stiffer than observed in the experiments. The comparison between numerical and experimental load-displacement diagrams is shown in Fig. 16. The experimental behavior is reproduced satisfactorily and the collapse load can be estimated within a 15% range of the experimental values. The sudden load drops are due to cracking in a single integration point of the potential cracks in a brick and opening of each complete crack across one brick (note that, when a potential vertical crack is almost complete across one brick, relatively high shear stresses are set to zero in a single step). In the former case a mesh refinement is likely to smooth the curve but, in the latter, a snap through or snap back will, as in case of the hollow walls, most certainly be found. Here, these points were sporadically "jumped over" in the analysis by the use of a secant stiffness instead of a tangent stiffness, only for the discrete cracking criterion in the bricks.

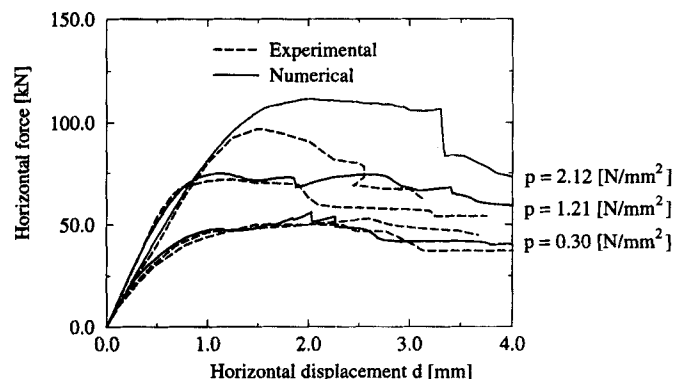


**FIG. 16. Load-Displacement Diagrams for Solid Walls**

TOTAL DISPLACEMENTS

DAMAGE

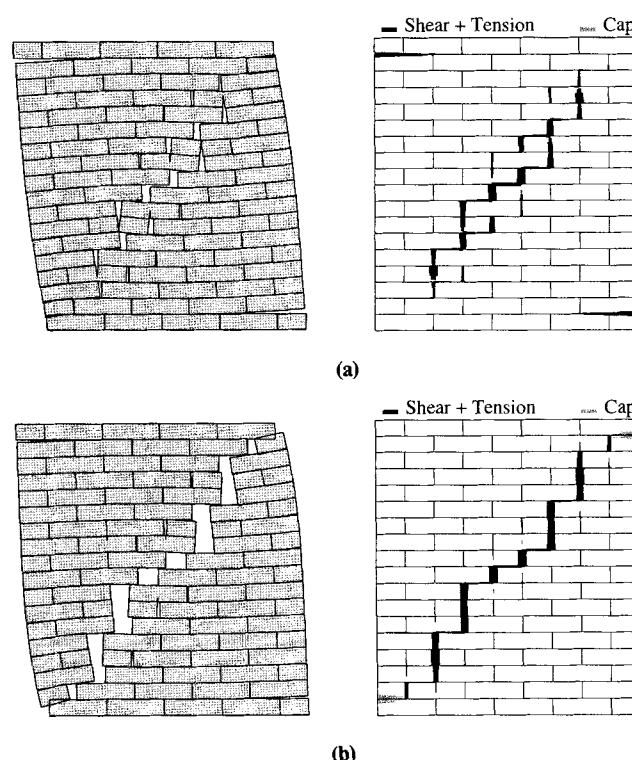


**FIG. 17. Numerical Results at Horizontal Displacement  $d$  (Solid Walls): (a)  $d = 2.0$  mm; (b)  $d = 4.0$  mm**

For the interface cap model, the consistent tangent operator was used throughout the analysis.

The wall with an initial vertical load of  $0.30 \text{ N/mm}^2$  was chosen for further discussion because two specimens were built. The behavior of the wall is well captured by the model as illustrated in Fig. 17. Initially, two horizontal tension cracks develop at the bottom and the top of the wall. A stepped diagonal crack through head and bed joints immediately follows (see Fig. 17a). This crack starts in the middle of the wall and is accompanied by initiation of cracks in the bricks. Under increasing deformation, the crack progresses in the direction of the supports and, finally, a collapse mechanism is formed with crushing of the compressed toes and a complete diagonal crack through joints and bricks (see Fig. 17b).

## CONCLUSIONS

The present paper contains some computational results of a research program aiming at development of rational and robust numerical techniques for the analysis of masonry structures. At this first stage a micromodeling strategy, in which the units and joints are separately discretized, is considered.

An interface cap model that includes all the possible failure mechanisms of masonry structures has been developed. The composite yield surface is implemented in an accurate and robust algorithm. The fully implicit Euler backward return mapping is solved with a Newton-Raphson technique for all modes of the cap model, including the corners. Tangent operators, consistent with the integration algorithm are derived for all the modes of the cap model. Isotropic coupling is assumed between tensile softening and decohesion. Application of the model to experiments on shear-walls shows good agreement and provides additional knowledge about the behavior of masonry structures. The model is able to reproduce the complete path of the structures until total degradation without numerical difficulties. It is further noted that within the tolerance adopted for the satisfaction of the return mapping ( $10^{-7}$  of the initial violation of the yield criteria), no inaccurate points are found during the large scale analyses. The global convergence for the analyses using exclusively the interface cap model detailed in this article also behaves extremely well (typically 3 to 4 global iterations are needed to reach an energy norm of  $10^{-6}$ ). Finally, it is shown that the modeling strategy adopted is mesh insensitive.

The writers believe that the importance of numerical modeling for supporting safe and economic designs of masonry structures is already evident from the present article. For a thorough interpretation of the behavior of the shear walls presented herein the reader is referred to Lourenço and Rots (1994).

## ACKNOWLEDGMENTS

The models reported in the present paper have been implemented in the DIANA finite element code, which is a registered trademark of TNO Building and Construction Research. The research is supported financially by the Netherlands Technology Foundation (STW) under grant DCT 33.3052 and the Netherlands brick industries via CUR committees C96 and A33 on Structural Masonry.

## APPENDIX. REFERENCES

- Atkinson, R. H., and Yan, G. G. (1990). "Results of a statistical study of masonry deformability." *Masonry Soc. J.*, 9(1), 81–90.
- de Borst, R., and Feenstra, P. H. (1990). "Studies in anisotropic plasticity with reference to the Hill criterion." *Int. J. Numer. Methods Engrg.*, 29, 315–336.
- Drucker, D. C., Gibson, R. E., and Henkel, D. J. (1957). "Soil mechanics and work hardening theories of plasticity." *Trans.*, ASCE, 122, 338–346.
- Hofstetter, G., Simo, J. C., and Taylor, R. L. (1993). "A modified cap model; closest point solution algorithms." *Comp. & Struct.*, 46(2), 203–214.
- Hohberg, J.-M. (1992). "A joint element for the nonlinear dynamic analysis of arch dams." *Rep. No. 186*, Inst. of Struct. Engrg., ETH Zurich, Switzerland.
- Koiter, W. T. (1953). "Stress-strain relations, uniqueness and variational problems for elastic-plastic materials with a singular yield surface." *Quarterly Appl. Math.*, 11, 350–354.
- Lofti, H. R., and Shing, P. B. (1994). "Interface model applied to fracture of masonry structures." *J. Struct. Engrg.*, ASCE, 120(1), 63–80.
- Lourenço, P. B., and Rots, J. G. (1993). "On the use of micro-modelling for the analysis of masonry shear-walls." *Computer methods in structural masonry—2*, G. N. Pande and J. Middleton, eds., Book & Journals Int. Swansea, United Kingdom, 14–26.
- Lourenço, P. B., and Rots, J. G. (1994). "Understanding the behaviour of shear walls: a numerical review." *Proc., 10th Int. Brick/block Masonry Conf.*, N. G. Shrive and A. Huizer, eds., Calgary, Canada, 11–20.
- Lourenço, P. B., Rots, J. G., and Blaauwendraad, J. (1994). "Implementation of an interface cap model for the analysis of masonry structures." *Computational modelling of Concrete structures*, H. Mang, N. Bicanic, and R. de Borst, eds., Pineridge Press, Swansea, United Kingdom, 123–134.
- Mann, W., and Müller, H. (1982). "Failure of shear-stressed masonry—an enlarged theory, tests and application to shear walls." *Proc., British Ceramic Soc.*, 30, 223–235.
- Ortiz, M., and Popov, E. P. (1985). "Accuracy and stability of integration algorithms for elasto-plastic constitutive relations." *Int. J. Numer. Methods Engrg.*, 21, 1561–1576.
- Raijmakers, T. M. J., and Vermeltfoort, A. T. (1992). "Deformation controlled meso shear tests on masonry piers." *Rep. B-92-1156*, TNO-BOUW/TU Eindhoven, Build. and Constr. Res., Eindhoven, The Netherlands (in Dutch).
- Roscoe, K. H., and Burland, J. B. (1968). "On the generalized stress-strain behaviour of 'wet' clay." *Engineering plasticity*, J. Heyman and F. A. Lekie, eds., Cambridge University Press, London, England, 535–609.
- Rots, J. G. (1988). "Computational modelling of concrete fracture." Dissertation, Delft Univ. of Technology, Delft, The Netherlands.
- Simo, J. C., Kennedy, J. G., and Govindjee, S. (1988). "Non-smooth multisurface plasticity and viscoplasticity. Loading/unloading conditions and numerical algorithms." *Int. J. Numer. Methods Engrg.*, 26, 2161–2185.
- van der Pluijm, R. (1992). "Material properties and its components under tension and shear." *Proc., 6th Can. Masonry Symp.*, Saskatoon, Canada.
- van der Pluijm, R. (1993). "Shear behaviour of bed joints." *Proc., 6th North Am. Masonry Conf.*, Philadelphia, Pa., 125–136.
- Vermeltfoort, A. T., Raijmakers, T. M. J., and Janssen, H. J. M. (1993). "Shear tests on masonry walls." *Proc., 6th North Am. Masonry Conf.*, Philadelphia, Pa., 1183–1193.